Electronic Supplementary Information for

Spirobifluorene with an asymmetric fluorenylcarbazolamine electron-donor as the hole transport material increases thermostability and efficiency of perovskite solar cells

Yutong Ren,[a] Yuefang Wei,[a] Tianyu Li,[a] Yanfei Mu,[b] Min Zhang,[b] Yi Yuan,[a] Jing Zhang[a] and Peng Wang[a]*

[a] State Key Laboratory of Silicon and Advanced Semiconductor Materials, Department of Chemistry, Zhejiang University, Hangzhou, 310028, China

[b] Institute for New Energy Materials and Low Carbon Technologies, Tianjin University of Technology, Tianjin, 300384, China

*Corresponding author.
E-mail addresses: pw2015@zju.edu.cn (P. Wang).

1 Experimental section

1.1 Materials

2-Amino-9,9-dimethylfluorene (97%, Energy Chemical), 3-bromo-9-methyl-9*H*-carbazole (97%, Energy Chemical), tris(dibenzylideneacetone)dipalladium ($Pd_2(dba)_3$, 98%, Energy Chemical), bis(2-diphenylphosphinophenyl)ether (DPEphos, 98%, Energy Chemical), sodium *tert*-butoxide (NaO(*t*-Bu), 98%, Energy Chemical), 2,2',7,7'-tetrabromo-9,9'-spirobifluorene (97%, Energy Chemical), tri-*tert*-butylphosphine tetrafluoroborate (P(*t*-Bu)·HBF_4, 98%, Energy Chemical), 1-ethyl-3-methylimidazolium bis(trifluoromethanesulfonyl)imide (EMITFSI, 98%, Energy Chemical), bis(pentamethylcyclopentadienyl)iron (DMFc, 98%, ACROS), benzocyclobutene (BCB, 98%, Energy Chemical), toluene (99%, Sinopharm Chemical Reagent Co., Ltd), tetrahydrofuran (THF, extra dry, 99.9%, Energy Chemical), deuterated THF (THF-d_8, 99.8%, Energy Chemical), isopropanol (≥99.9%, Energy Chemical), chlorobenzene (99.8%, Acros Organics), 4-*tert*-butylpyridine (TBP, 96%, Aldrich), acetone (≥99.5%, Energy Chemical), ethanol (99.7%, Aladdin), tin oxide (SnO_2, 15% in H_2O colloidal dispersion, Alfa Aesar), PbI_2 (99.99%, TCI), RbCl (99.9%, 3A), formamidinium iodide (FAI, 99.0%, Greatcell Solar), methylammonium chloride (MACl, ≥99.5%, Xi'an Polymer Light Technology Corp.), dimethyl sulfoxide (DMSO, 99.9%, Aldrich), *N*,*N*-dimethylformamide (DMF, 99.8%, Aldrich), phenethylammonium iodide (PEAI, 98%, TCI), and the hole transport material spiro-OMeTAD (≥99.8%, Xi'an Polymer Light Technology Corp.) were all procured from commercial sources and used without additional purification. The preparation of 4-*tert*-butylpyridinium bis(trifluoromethanesulfonyl)imide (TBPHTFSI) and DM followed the previously reported methods.[1,2]

1.2 General characterization

The melting points were determined using a WRS-1B automatic digital melting point apparatus (Shanghai INESA Physico-Optical Instrument). The ^{1}H NMR and ^{13}C NMR spectra were recorded on an AVANCE III 400 NMR spectrometer (Bruker). The high-resolution mass spectra (HR-MS) were acquired on a 6545 LC/Q-TOF system (Agilent). The attenuated total reflection-Fourier transform infrared (ATR-FTIR) spectra were collected on a Vector 22 FTIR spectrometer (Bruker). The photoluminescence (PL) spectra and the time-resolved PL (TRPL) decays were obtained using a Life-Spec-II fluorescence spectrometer (Edinburgh Instruments Ltd). The cyclic voltametric (CV) measurements were conducted on a CHI660C electrochemical workstation (CH Instruments), using a three-electrode electrolytic cell, including a glassy carbon working electrode, a platinum foil counter electrode, and an Ag/AgCl (sat. KCl) auxiliary electrode, and the supporting electrolyte was 0.1 M of EMITFSI in THF solution. The thicknesses of the thin films were measured using a D-500 stylus profilometer (KLA-

Tencor). The differential scanning calorimetry (DSC) measurements were carried out using a DSC Q100 V9.7 Build 291 (TA) at a heating rate of 10 °C min^{-1} under a flowing nitrogen atmosphere. The water contact angles of the thin films were measured with a Dropmeter 100P contact angle meter. The transmission polarization optical microscope (POM) images were recorded using an SDPTOP CX40P system. The cross-sectional scanning images were acquired with a Helios NanoLab 460HP electron microscope (FEI). We used focused ion beam to cut out a very small hole in the sample for cross-sectional SEM imaging. This method normally results in visual deviation in the relative thickness of each layer of the sample. The top-viewed surface morphologies were observed with a SU-70 field emission scanning electron microscope (Hitachi). The fluorescence optical microscope (FOM) images were obtained with an ECLIPSE Ti-U system (Nikon). The X-ray diffraction (XRD) patterns were collected using a SmartLab diffractometer (Rigaku), operated at 7200 W power (40 kV, 180 mA), with Cu Kα radiation (λ=0.15418 nm).

1.3 *N*-(9,9-Dimethyl-9*H*-fluoren-2-yl)-9-methyl-9*H*-carbazol-3-amine

A dried Schlenk tube was charged with 2-amino-9,9-dimethylfluorene (2.1 g, 10 mmol), 3-bromo-9-methyl-9*H*-carbazole (2.6 g, 10 mmol), $Pd_2(dba)_3$ (183.1 mg, 0.2 mmol), DPEphos (215.4 mg, 0.4 mmol), NaO(*t*-Bu) (1.9 g, 20 mmol), and toluene (50 mL). The reaction tube was chilled, evacuated, and purged with argon three times. The reaction mixture was then refluxed under argon for 12 h. After cooling, the mixture was filtered through a Kieselguhr pad, and the filtrate was concentrated in vacuum. The resulting product was purified by column chromatography (THF/petroleum ether 60–90 °C, *v*/*v*, 1/3) on silica gel, yielding a white solid of the desired product **FC** (3.4 g, 88% yield). Melting point: 202–204 °C. ^{1}H NMR (400 MHz, THF-d_8) δ: 7.87 (d, *J*=7.9 Hz, 1H), 7.79 (s, 1H), 7.40 (m, 2H), 7.31–7.16 (m, 6H), 7.06 (t, *J*=7.5 Hz, 1H), 7.00–6.95 (m, 3H), 6.79 (dd, *J*=8.3, 1.7 Hz, 1H), 3.79 (s, 3H), and 1.50 (s, 6H) ppm. ^{13}C NMR (100 MHz, THF-d_8) δ: 156.16, 153.82, 147.76, 142.74, 141.10, 138.49, 136.56, 131.01, 127.68, 126.44, 126.12, 124.52, 123.74, 123.12, 121.69, 121.55, 120.97, 119.33, 119.31, 114.85, 113.11, 109.97, 109.92, 109.45, 47.39, 29.29, and 27.91 ppm. HR-MS (ESI) *m/z* calculated for $[M+H]^+$: 389.2012. Found: 389.2011. ATR-FTIR (film) ν_{max}=2965, 1611, 1489, 1310, 1242, 1153, 1065, 864, and 738 cm^{-1}.

1.4 *N*²,*N*²',*N*⁷,*N*⁷'-Tetrakis(9,9-dimethyl-9*H*-fluoren-2-yl)-*N*²,*N*²',*N*⁷,*N*⁷'-tetrakis(9-methyl-9*H*-carbazol-3-yl)-9,9'-spirobi[fluorene]-2,2',7,7'-tetraamine

A dried Schlenk tube was charged with 2,2',7,7'-tetrabromo-9,9'-spirobifluorene (505.6 mg, 0.8 mmol), **FC** (1.4 g, 3.6 mmol), $Pd_2(dba)_3$ (36.6 mg, 0.04 mmol), P(*t*-Bu)·HBF_4 (23.2 mg, 0.08 mmol), NaO(*t*-Bu) (615.0 mg, 6.4 mmol), and toluene (50 mL). The reaction tube was then chilled, evacuated, and purged with argon three times.

The reaction mixture was refluxed under argon for 24 h. After cooling, the mixture was filtered through a Kieselguhr pad, and the filtrate was concentrated in vacuum. The resulting product was purified by column chromatography (THF/petroleum ether 60–90 °C, *v*/*v*, 1/1) on silica gel to yield the desired product **SBF-FC**, as a faint yellow solid (1.3 g, 87% yield). Melting point: >300 °C. ^{1}H NMR (400 MHz, THF-d_8) δ: 8.01 (d, *J*=1.9 Hz, 4H), 7.97 (d, *J*=7.9 Hz, 4H), 7.56 (d, *J*=7.4 Hz, 4H), 7.52 (d, *J*=8.4 Hz, 4H), 7.45–7.31 (m, 16H), 7.31–7.25 (m, 12H), 7.20–7.04 (m, 12H), 6.99–6.90 (m, 8H), 6.78 (dd, *J*=8.5, 2.2 Hz, 4H), 3.78 (s, 12H), and 1.55 (s, 24H) ppm. ^{13}C NMR (100 MHz, THF-d_8) δ: 155.78, 154.51, 151.19, 149.33, 148.49, 142.83, 140.63, 140.33, 139.67, 136.40, 134.06, 127.77, 127.01, 126.74, 126.70, 124.96, 123.75, 123.27, 122.95, 122.61, 121.48, 121.37, 120.80, 120.09, 119.80, 119.78, 117.78, 117.49, 110.56, 109.54, 47.69, 29.37, and 27.90 ppm. HR-MS (ESI) *m/z* calculated for $[M]^+$: 1861.8418. Found: 1861.8404. ATR-FTIR (film) ν_{max}=2958, 1603, 1462, 1311, 1272, 1121, 1065, 811, and 735 cm^{-1}.

1.5 Conductivity

We deposited a hole transport layer onto interdigital gold electrodes by spin-coating a chlorobenzene solution at 1000 rpm. The solution consists of 132 mM of TBP, 50 mg mL^{-1} of HTM and TBPHTFSI at a concentration of 0, 2.6, 5.6, or 8.8 mg mL^{-1}. The interdigital gold electrode comprises 119 channels, each with a length (L) of 1.5 mm, a width (W) of 10 μm, and a thickness (t) of 110 nm. Prior to measuring the current–voltage (*I–V*) curve with a Keithley 2400 source meter, we stored the sample in dry air (<5% RH) for seven days. The *I–V* curve was measured in the voltage range from –1.0 V to 1.0 V. The direct-current conductivity (σ) can be calculated by

$$\sigma = s\frac{W}{nLt}, \tag{1}$$

where s is the slope derived from the linear fitting of the *I–V* curve and n is the channel number. Note that, the σ of the hole transport layer can reach a steady state after being stored in dry air for about five days and remained constant thereafter, suggesting that air doping has reached an equilibrium.

1.6 Hole density

We first utilized a metal-insulator-semiconductor (MIS) device to quantify the hole density of the hole transport layer, which is exclusively composed of HTM. The MIS device architecture consists of n^{++}-Si/SiO_2/p-BCB/HTL/Au, where p-BCB denotes polybenzocyclobutene. A p-BCB layer was grown on heavily n-type doped Si with a 300 nm SiO_2 coating via annealing a BCB layer at 250 °C for 1 h. A 1 mg mL^{-1} solution of BCB in CB was spin-coated to deposit the BCB layer. The HTL was deposited onto the p-BCB layer by spin-coating, followed

by vacuum deposition of the gold layer. The AutolabPGSTAT302N electrochemical workstation was used to measure the impedance spectra of the MIS device at various bias potentials (V). The capacitance (C) was computed using the equation,

$$C = -\frac{1}{\omega}\left[\frac{Z'' - \omega L_i}{(Z' - R_s)^2 + (Z'' - \omega L_i)^2}\right], \quad (2)$$

where Z' and Z'' denote the real and imaginary parts of the impedance spectra, respectively. R_s represents the series resistance, L_i denotes the parasitic inductance, and ω is the angular frequency. The C–V features distinctly demonstrated the accumulation regime and depletion regime of the semiconductor layer. Subsequently, the hole density (p) was computed by,

$$p = \frac{2}{q\varepsilon_r\varepsilon_0 \frac{d(A/C)^2}{dV}}, \quad (3)$$

where q represents the elementary charge, ε_r refers to the relative permittivity, ε_0 denotes the vacuum permittivity, and A is the area of the MIS device.

In subsequent experiments, determining the hole density of hole transport layers containing TBPHTFSI using the MIS device was found to be a challenge. To overcome this hurdle, we employed a comparison approach using the quadratic integral intensity of the electron paramagnetic resonance (EPR) signal of the hole transport layer with or without TBPHTFSI to estimate its hole density, given the known density of the layer without TBPHTFSI. Specifically, a HTL was spin-coated onto a 2 cm × 2 cm microslide and stored in dry air for seven days. The resulting sample was then crushed and loaded into a borosilicate glass tube for EPR measurement using a Bruker A300-10/12 spectrometer.

1.7 Solar cell fabrication

We prepared perovskite solar cells utilizing the device architecture of ITO/SnO_2/$FAPbI_3$/HTL/Au. The ITO glass was initially laser-etched, and then underwent a sequence of ultrasonic cleanings with a detergent, deionized water, acetone, and ethanol. The cleaned ITO substrate was subsequently treated with ultraviolet ozone. For the electron transport layer, a 3% by weight SnO_2 colloid solution was spin-coated onto the ITO substrate and subjected to heating at 150 °C for 30 min. Following this, a DMF/DMSO (volume ratio of 9:1) solution containing 1.5M PbI_2 and 0.075M RbCl was spin-coated onto the electron transport layer and heated at 70 °C for 1 min. After cooling to room temperature, an isopropanol solution containing 90 mg mL^{-1} of FAI and 13.5 mg mL^{-1} of MACl was spin-coated and heated at 150 °C for 30 min to create the $FAPbI_3$ perovskite layer, which included a small amount of $(PbI_2)_2RbCl$.[3] An interface layer was subsequently deposited by spin-coating a 5 mg mL^{-1} PEAI

isopropanol solution, followed by the deposition of an HTL using a chlorobenzene solution containing 50 mg mL^{-1} HTM, 8.8 mg mL^{-1} TBPHTFSI, and 132 mM TBP at 5000 rpm. Finally, an 80 nm thick gold electrode was deposited to complete the device fabrication, using thermal evaporation under a vacuum of less than 10^{-4} Pa.

1.8 Photocurrent–voltage and external quantum efficiency

The AM1.5G sunlight at an irradiation of 100 mW cm^{-2} was supplied by an LS1000-4S-AM solar simulator (Solar Light Company, USA). The photocurrent density–voltage (*J–V*) curves were determined using a Keithley 2400 source meter in conjunction with Labview 14.0. The photoactive area of perovskite solar cells was defined by a metal mask with an aperture area of 0.16 cm^2. External quantum efficiency (EQE) measurement was performed using an Omni-λ300 monochromator (Zolix, China) in conjunction with a 150 W xenon lamp (Zolix, China) to provide monochromatic light. Photocurrent was recorded by employing a computer controlled Keithley 2400 source meter. Monochromatic light intensity was measured using a Hamamatsu S1337-1010BQ silicon diode that was calibrated at the National Institute of Metrology, China.

1.9 Operation stability and thermostability

We utilized a 16-channel photovoltaic tracking system (YH Electronic Equipment Business) and an SLS-LED-80A solar simulator (Qingdao Solar Scientific Instrument High-tech Co., LTD) to conduct maximum power point (MPP) tracking of perovskite solar cells within a nitrogen-filled glovebox. MPP data were collected at two-minute intervals using the standard perturb and observe method. To evaluate the thermostability of perovskite solar cells, we subjected them to an FD56 oven (Binder, Germany) at 85 °C. After a specific period, the cells were taken out and their *J–V* characteristics were measured in dry air at room temperature, under AM1.5G conditions. The atmospheric humidity of the oven was between 40% and 90%.

2 Theoretical modelling

2.1 Frontier molecular orbital and reorganization energy of hole Extraction

The molecular geometry optimization was carried out using the Gaussian 16 program suite by the density functional theory (DFT) method at the B3LYP/6-311G(d,p) level. The impact of THF was modeled using IEFPCM. Frontier molecular orbitals were visualized using GaussView 6. In accordance with the semi-classical Marcus electron transfer theory, the rate (ω_{ij}) of hole extraction from the photoexcited perovskite (i) to the hole transport layer (j) is dependent of the transfer integral (v_{ij}), the driving force (ΔG_0), and the reorganization energy (λ_{he}). λ_{he} can be expressed as the sum of internal reorganization energy (λ_{int}) and external reorganization energy (λ_{out}). However, it is noteworthy that the contribution of λ_{out} is negligible in the solid state. Similarly, the

λ_{int} associated with perovskite is also insignificant. Using the energies on adiabatic potential surfaces, λ_{he} can be estimated roughly by the approximation relation $\lambda_{he} \approx E_+^* - E_+$, where E_+^* and E_+ refer to the energies of the ion in neutral geometry and the ion in ion geometry. λ_{he} was also calculated by the DFT method at the B3LYP/6-311G(d,p) level.

2.2 Hole transport in amorphous organic solid

In amorphous organic solids, the transport of holes can be described by the hopping mechanism. The hopping rate (ω_{ij}) depends on the transfer integral (v_{ij}) between the i and j hopping sites, the HOMO difference (ΔE_{ij}) between them, and the reorganization energy (λ_{ht}) associated with hole transport. We first computed λ_{ht} by the DFT method at the B3LYP/6-311G(d,p) level. Next, we utilized the Amorphous Cell in the Materials Studio 8.0, to construct a cubic box with periodic boundaries, which consists of 360 HTM molecules. We further conducted molecular dynamics (MD) simulations using the COMPASS II force field to obtain the microstructure of the amorphous box. The neighbor lists were picked up from the box, each of which contains a pair of molecules fulfilling the selection rule that the two molecules have a nearest atom-to-atom distance of ≤5 Å. The centroid distance (*d*) of each neighbor list was also extracted. The Thole model was utilized to assess the electrostatic and polarization contributions to ΔE_{ij}, and the DFT calculations at the CAM-B3LYP/6-311G(d,p) level were employed to obtain the partial charges of the molecules in their neutral and cationic states. The energetic disorder was extracted using the Gaussian disorder model, which involved fitting the profile of ΔE_{ij}. For each neighbor list, an approximate method based on ZINDO was used to compute v_{ij}, which was shown to produce consistent results with those obtained at the B3LYP/6-311G(d,p) level.[4] Lastly, the VOTCA toolkit was employed to conduct the stochastic kinetic Monte Carlo (kMC) simulations to yield the hole mobility.

2.3 Glass transition, diffusion coefficient, and permeability coefficient

We also utilized the Amorphous Cell in the Materials Studio 8.0, to construct a cubic box with periodic boundaries, which comprises 360 HTM molecules and additional TBPHTFSI molecules in a weight ratio of 85:15, and conducted MD simulations using the COMPASS II force field. Furthermore, we performed a series of simulations utilizing the FORCITE module in Materials Studio 8.0, to simulate the glass transition temperature (T_g) and diffusion coefficient (D). Initially, an NVT simulation was conducted at 700 K using a Nose thermostat, followed by an NPT simulation at the same temperature using both a Nose thermostat and a Berendsen barostat. Subsequently, we systematically lowered the temperature from 700 K to 200 K at an interval of 20 K, performing the NVT and NPT simulations at each temperature. The equilibrated specific volume (SV) was recorded at each

temperature and subjected to linear fitting. By identifying the intersection of the resulting lines in the low and high temperature regions, we determined the theoretical T_g, which is expressed by T_g^{SV}. Moreover, we added extra molecules of H_2O or HI to a TBPHTFSI containing composite, and performed the NVT and NPT simulations. We extracted the mean square displacements of intrinsic and extrinsic species by recording their trajectories to obtain D. The Sorption module in Materials Studio 8.0 was used to conduct a grand canonical Monte Carlo simulation on the adsorption isotherm of an amorphous box, obtaining the solubility coefficient (S) of H_2O or HI. Finally, the permeability coefficient of gas molecules (P) was determined using the formula $P = D \times S$.

3 Additional data

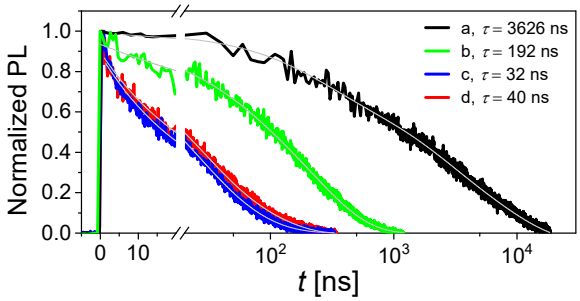

Fig. S1 Time-resolved photoluminescence (PL) traces for (a) $FAPbI_3$ on glass, (b) $FAPbI_3$ on SnO_2, (c) spiro-OMeTAD-coated $FAPbI_3$ on glass, and (d) SBF-FC-coated $FAPbI_3$ on glass. The gray lines represent biexponential fits of the normalized PL as a function of time (t), with PL lifetimes (τ) indicated.

Table S1 Parameters for fitting TRPL decays, time constants, and charge separation yields[a]

Sample	τ_1 [ns]	A_1	τ_2 [ns]	A_2	τ [ns]	ϕ_{CS} [%]
glass/$FAPbI_3$	481.8	0.37	5473.3	0.63	3626.4	/
ITO/SnO_2/$FAPbI_3$	43.2	0.23	236.2	0.77	191.8	94.7
glass/$FAPbI_3$/spiro-OMeTAD	18.4	0.54	48.8	0.46	32.4	99.1
glass/$FAPbI_3$/SBF-FC	19.5	0.58	69.1	0.42	40.3	98.9

[a]TRPL decays were fitted by a biexponential function. The parameters τ_1 and τ_2 denote the time constants associated with fast and slow decays, respectively, whereas A_1 and A_2 represent the relative amplitudes of these decays. The amplitude-averaged time constant, denoted by τ, can be computed using equation $\tau = A_1\tau_1 + A_2\tau_2$, please see Page 173 of ref 5. The yield of charge separation resulting from either electron extraction or hole extraction is denoted by ϕ_{cs}. The yield of charge separation due to electron extraction can be determined by

employing equation $\phi_{ee} = \frac{\tau_{glass} - \tau_{SnO_2}}{\tau_{glass}}$, where τ_{glass} represents the amplitude-averaged time constant of $FAPbI_3$ on glass, while τ_{SnO_2} corresponds to that of $FAPbI_3$ on SnO_2. On the other hand, the yield of charge separation due to hole extraction can be estimated using equation $\phi_{he} = \frac{\tau_{glass} - \tau_{HTL}}{\tau_{glass}}$, where τ_{HTL} refers to the amplitude-averaged time constant of HTL-coated $FAPbI_3$ on glass.

Table S2 Parameters related to hole extraction[a]

HTM	E_H^{CV} [eV]	E_H^{DFT} [eV]	λ_{he} [meV]
spiro-OMeTAD	–5.10	–4.74	87
SBF-FC	–5.06	–4.69	76

[a] E_H^{CV} denotes to the HOMO energy level derived through cyclic voltametric measurement, and E_H^{DFT} refers to the HOMO energy level calculated by the DFT method. λ_{he} represents the reorganization energy of hole extraction calculated by the DFT method.

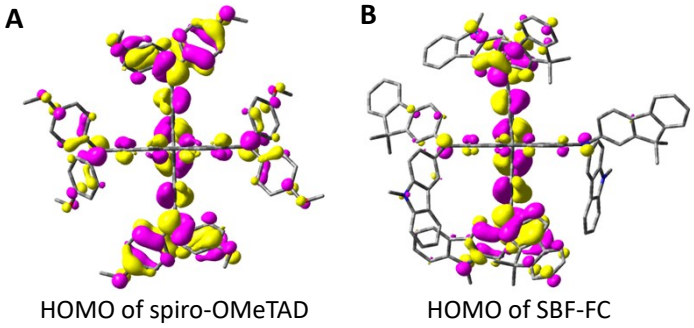

Fig. S2 Contour plots of HOMOs with an isovalue of 0.02.

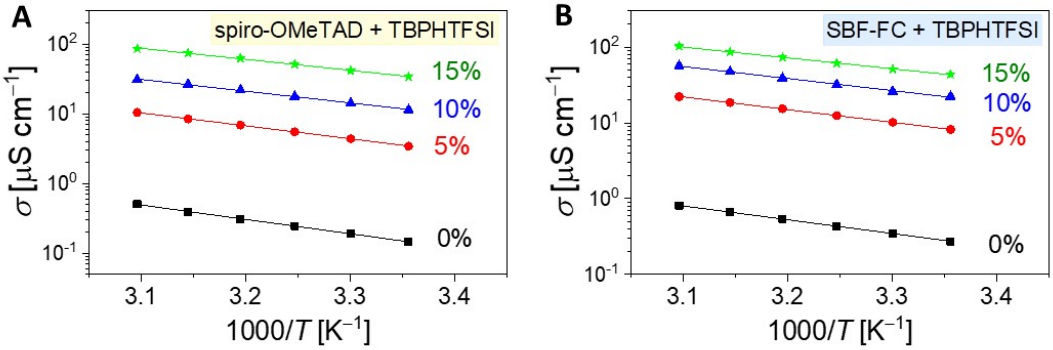

Fig. S3 Arrhenius plots of the electrical conductivity (σ) of (A) spiro-OMeTAD and (B) SBF-FC based HTLs with and without TBPHTFSI. The weight percentages of TBPHTFSI in the HTLs are indicated.

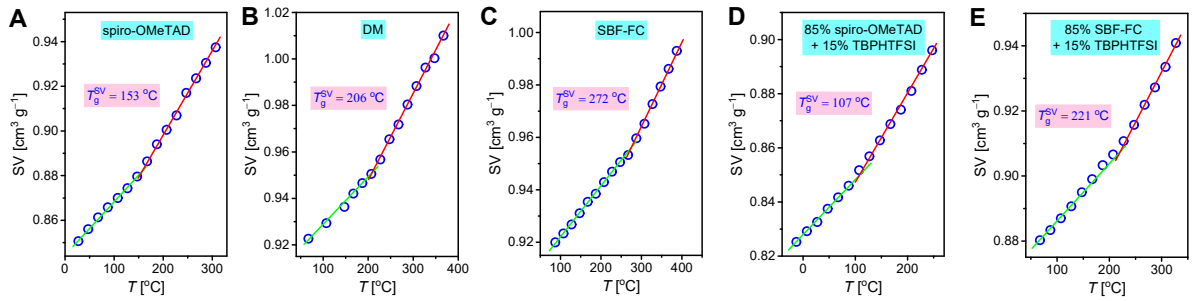

Fig. S4 Plots of the specific volume (SV) as a function of temperature (T), obtained from molecular dynamics simulation. The green and magenta lines depict the linear fits of the low-temperature and high-temperature regions, respectively. The theoretical glass transition temperature (T_g^{SV}) can be determined by the intersection of the linear fits.

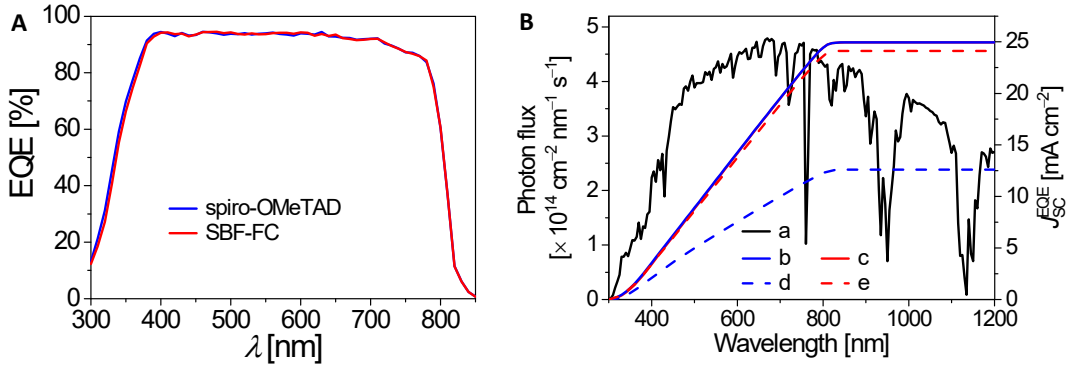

Fig. S5 (A) External quantum efficiency (EQE) spectra and (B) the ASTM G173 AM1.5G spectral photon flux (a). Panel B also presents the photocurrent densities predicted from the EQE spectra (J_{SC}^{EQE}) of the cell with spiro-OMeTAD (b), the cell with SBF-FC (c), the aged cell with spiro-OMeTAD (d), and the aged cell with SBF-FC (e). The aging was performed at 85 °C for 500 h.

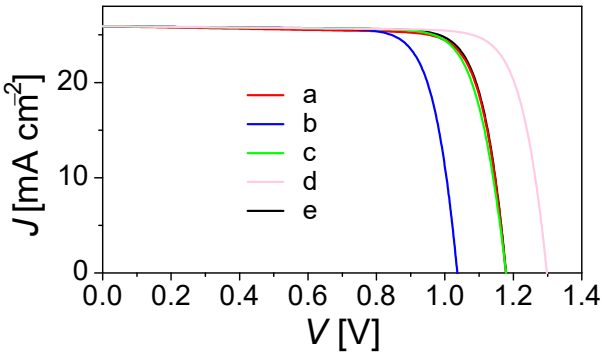

Fig. S6 Simulation of *J*–*V* curves based on the Shockley diode equation to quantify the impact of individual parameters (R_{sh}, I_s, R_s, or n) on both V_{OC} and FF. To achieve this, we generated a new *J*–*V* curve by incorporating one fitting parameter (a) R_{sh}, (b) I_s, (c) R_s, or (d) n from the *J*–*V* data of the spiro-OMeTAD cell, while maintaining the other three fitting parameters from the *J*–*V* data of the SBF-FC cell. Curve (e) corresponds to the *J*–*V* data of the SBF-FC cell and is presented for comparation.

Table S3 Parameters employed in *J*–*V* simulation and photovoltaic parameters inferred from simulated *J*–*V* characteristics[a]

Simulation parameters					Photovoltaic parameters			
R_{sh} [kΩ]	I_s [A]	R_s [Ω]	n	I_{ph} [10^{-3} A]	J_{SC} [mA cm^{-2}]	V_{OC} [V]	FF [%]	PCE [%]
17.9	2.9E-14	5.5	1.78	4.14	25.9	1.179	81.1	24.78
9.8	2.9E-14	5.5	1.78	4.14	25.9	1.178	80.2	24.49
17.9	6.5E-13	5.5	1.78	4.14	25.9	1.036	79.5	21.34
17.9	2.9E-14	9.4	1.78	4.14	25.9	1.179	79.9	24.40
17.9	2.9E-14	5.5	1.96	4.14	25.9	1.298	81.1	27.29

[a]The red marker denotes the simulation parameter obtained from the measured *J*–*V* data of the cell with spiro-OMeTAD, while the blue markers indicate the simulation parameters derived from the measured *J*–*V* data of the cell with SBF-FC.

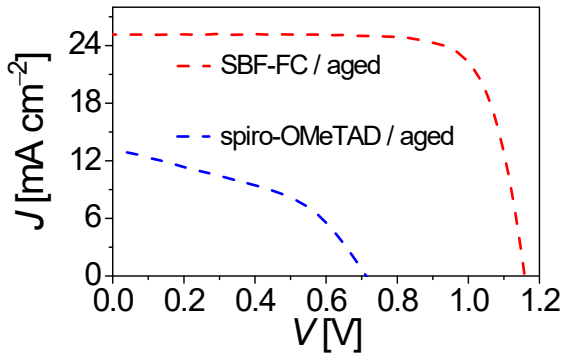

Fig. S7 Current density–voltage (*J*–*V*) characteristics of the aged cells measured under AM1.5G conditions. The aging was carried out at 85 °C for 500 h.

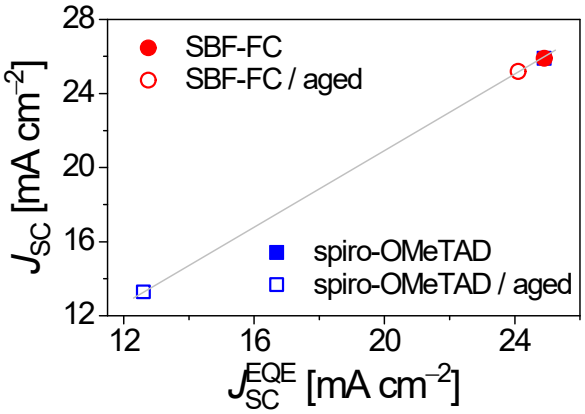

Fig. S8 The relation between J_{SC} and J_{SC}^{EQE}.

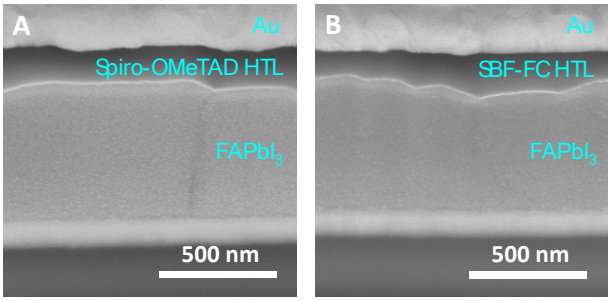

Fig. S9 Cross-sectional SEM images of the solar cells with (A) spiro-OMeTAD and (B) SBF-FC before aging.

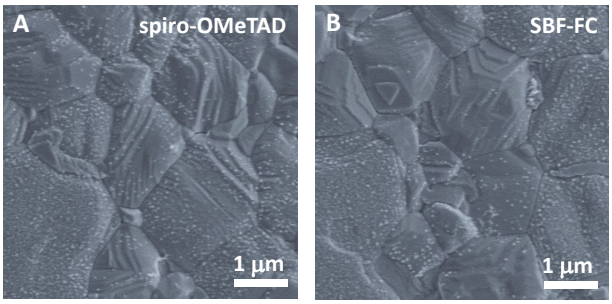

Fig. S10 Top-viewed SEM images of the perovskite layer in the solar cells before aging. The gold electrode and hole transport layer were removed prior to measurement.

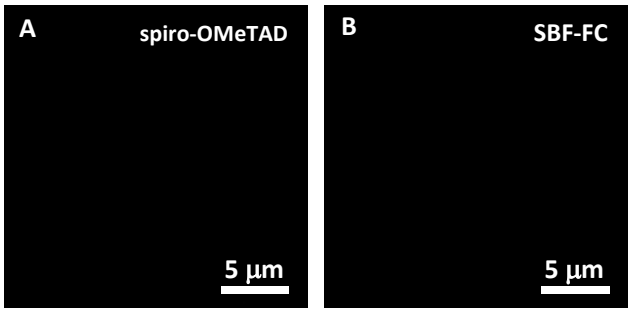

Fig. S11 Fluorescence optical microscopy images of the perovskite layer in the solar cells before aging. The gold electrode and hole transport layer were removed prior to measurement.

4 References

1 Y. Ren, M. Ren, X. Xie, J. Wang, Y. Cai, Y. Yuan, J. Zhang and P. Wang, *Nano Energy*, 2021, **81**, 105655.

2 N. J. Jeon, H. Na, E. H. Jung, T.-Y. Yang, Y. G. Lee, G. Kim, H.-W. Shin, S. I. Seok, J. Lee and J. Seo, *Nat. Energy*, 2018, **3**, 682.

3 Y. Zhao, F. Ma, Z. Qu, S. Yu, T. Shen, H.-X. Deng, X. Chu, X. Peng, Y. Yuan, X. Zhang and J. You, *Science*, 2022, **377**, 531.

4 V. Rühle, A. Lukyanov, F. May, M. Schrader, T. Vehoff, J. Kirkpatrick, B. Baumeier and D. Andrienko, *J. Chem. Theory Comput.*, 2011, **7**, 3335.

5 B. Valeur, *Molecular Fluorescence: Principles and Applications*, Wiley, 2001.

5 Appendix: ^{1}H NMR spectra, ^{13}C NMR spectra, mass spectra, and infrared spectra

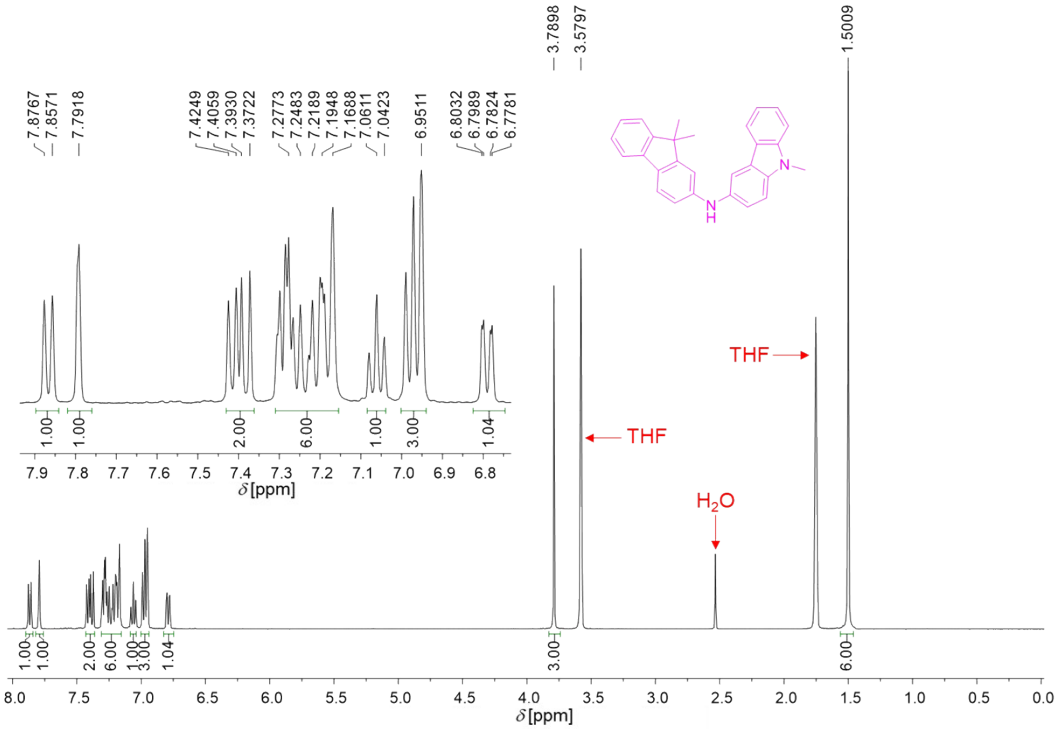

Fig. S12 ^{1}H NMR (400 MHz) spectrum of **FC** in THF-d_8.

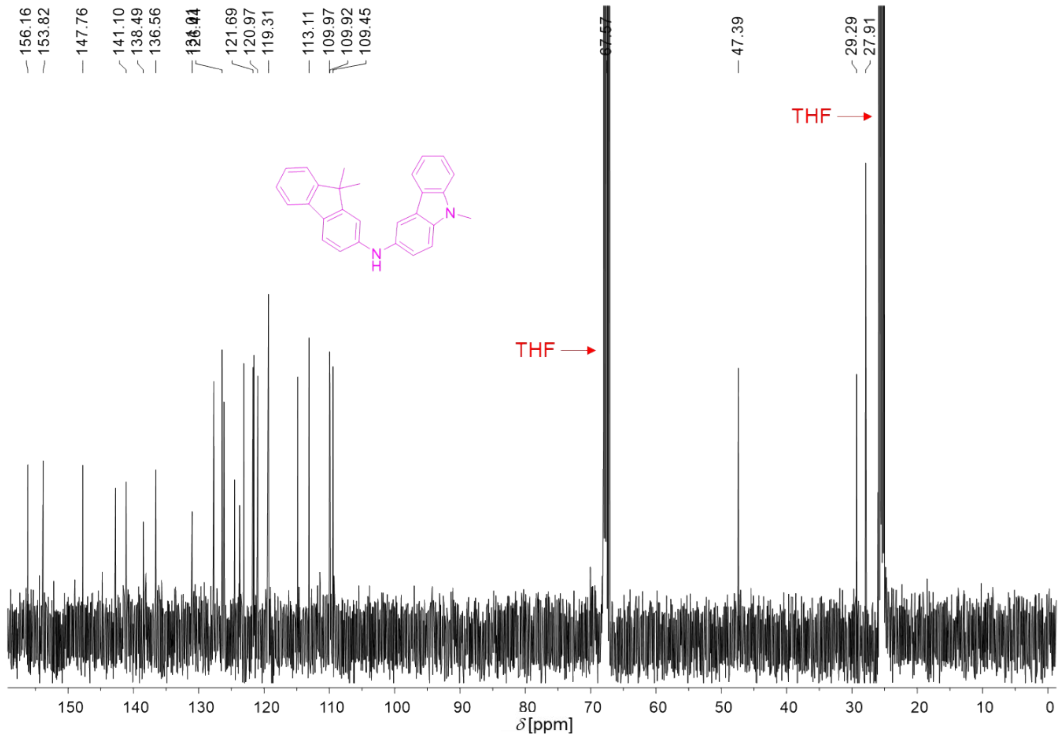

Fig. S13 ^{13}C NMR (100 MHz) spectrum of **FC** in THF-d_8.

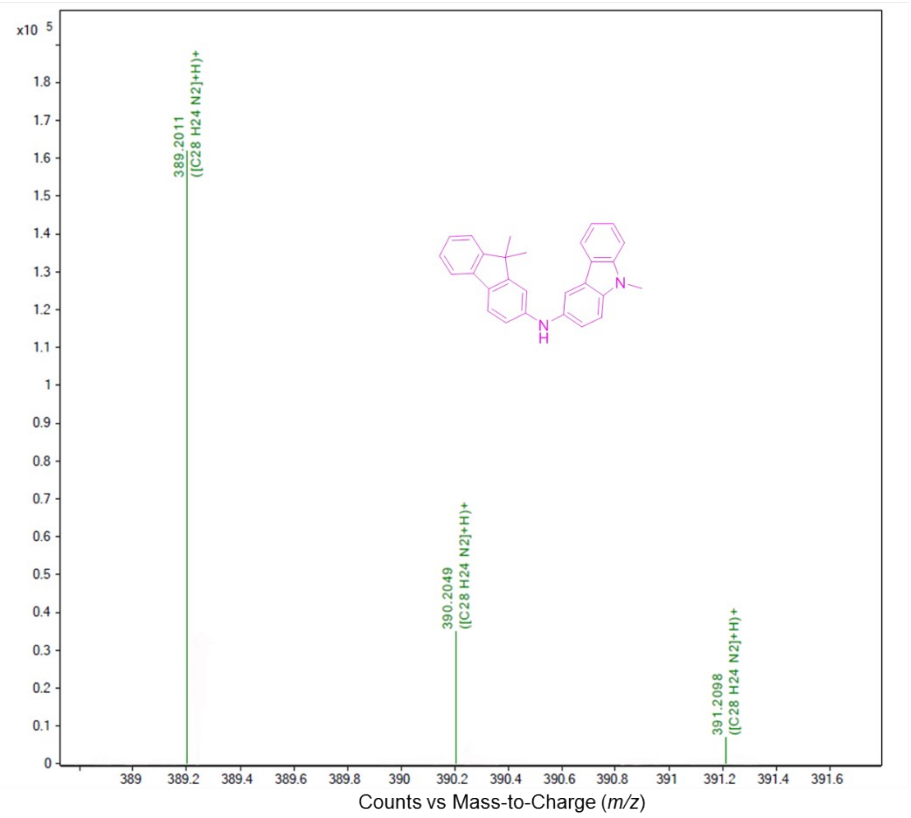

Fig. S14 High-resolution mass spectrum (ESI) of **FC**.

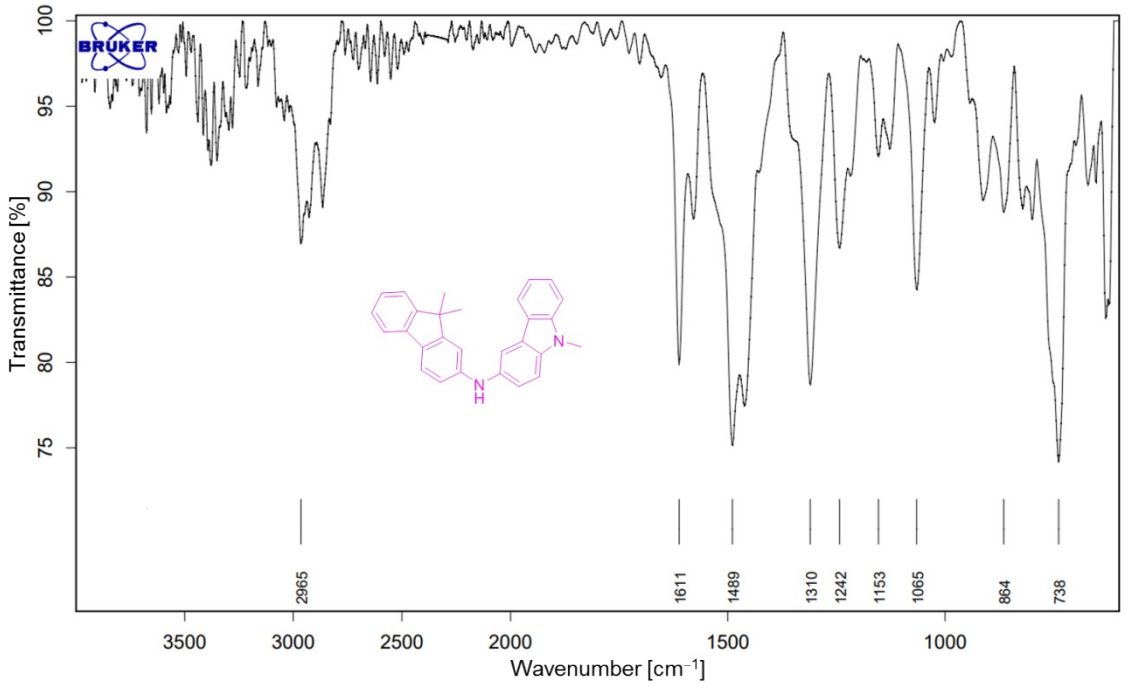

Fig. S15 ATR-FTIR spectrum of **FC**.

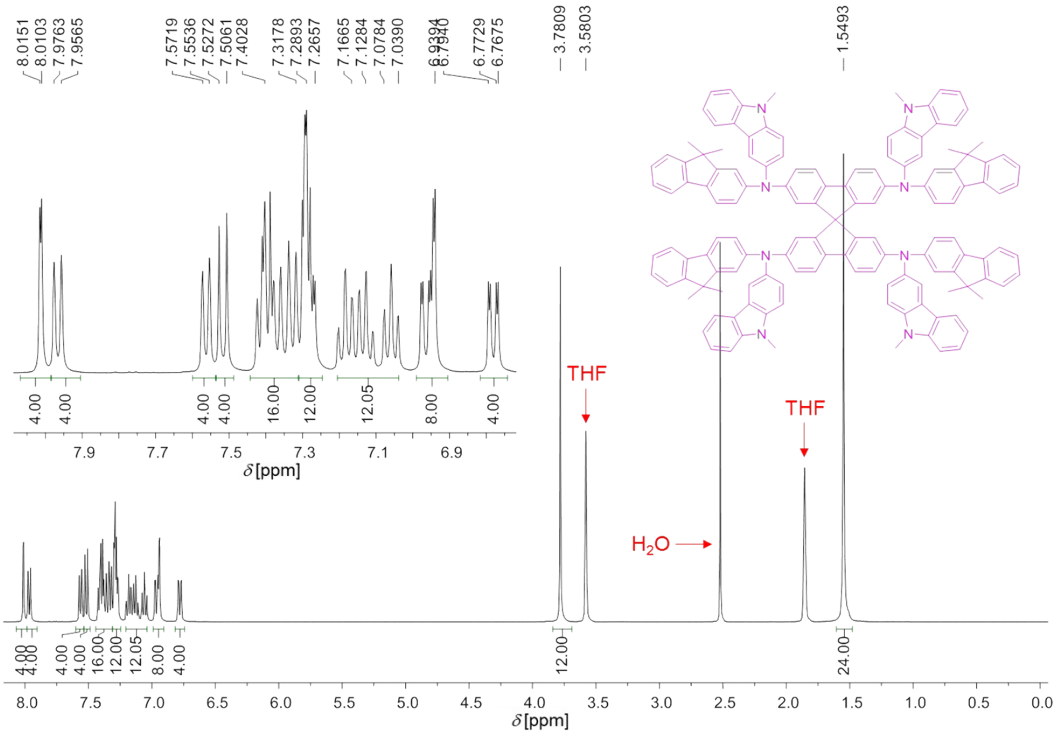

Fig. S16 ^{1}H NMR (400 MHz) spectrum of **SBF-FC** in THF-d_8.

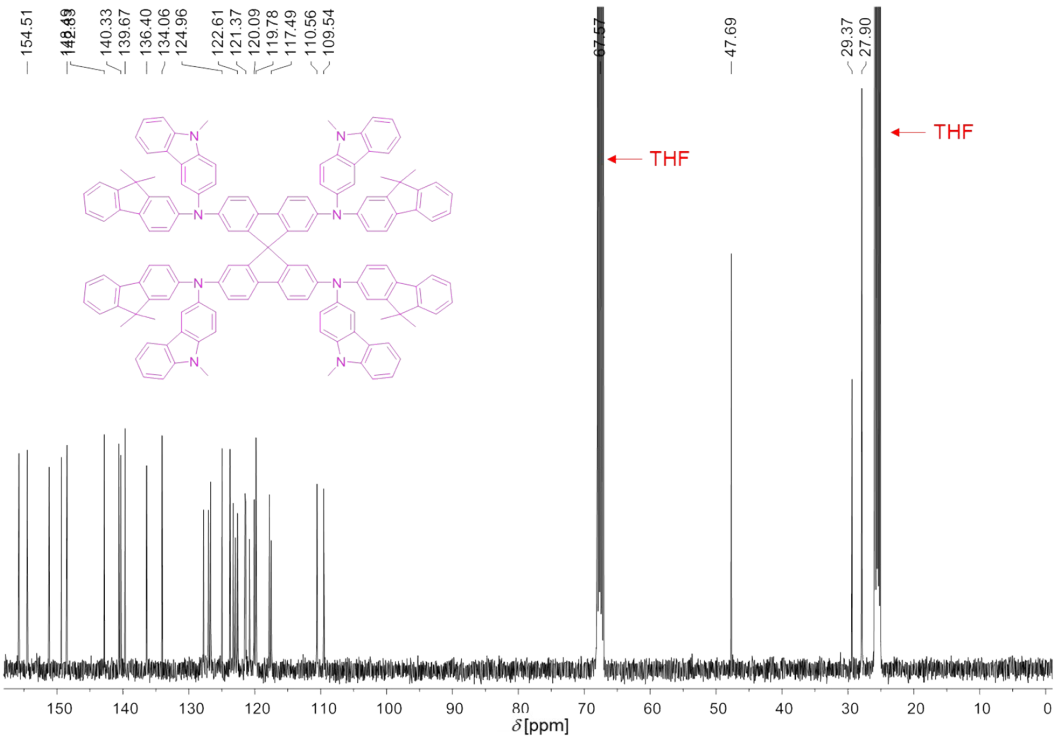

Fig. S17 ^{13}C NMR (100 MHz) spectrum of **SBF-FC** in THF-d_8.

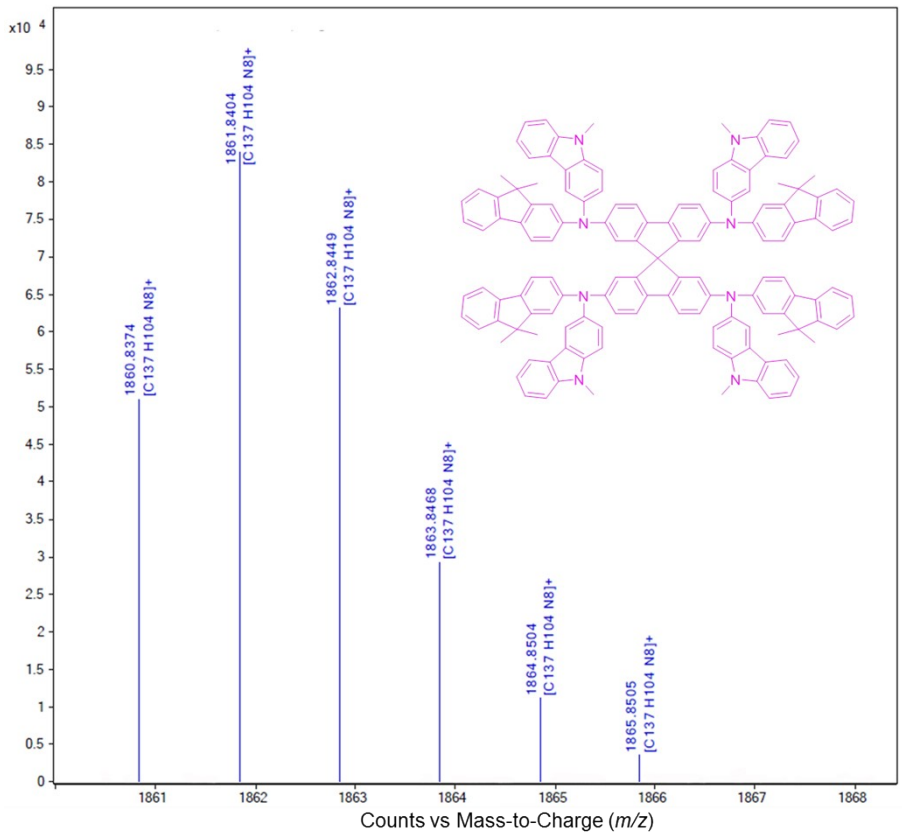

Fig. S18 High-resolution mass spectrum (ESI) of **SBF-FC**.

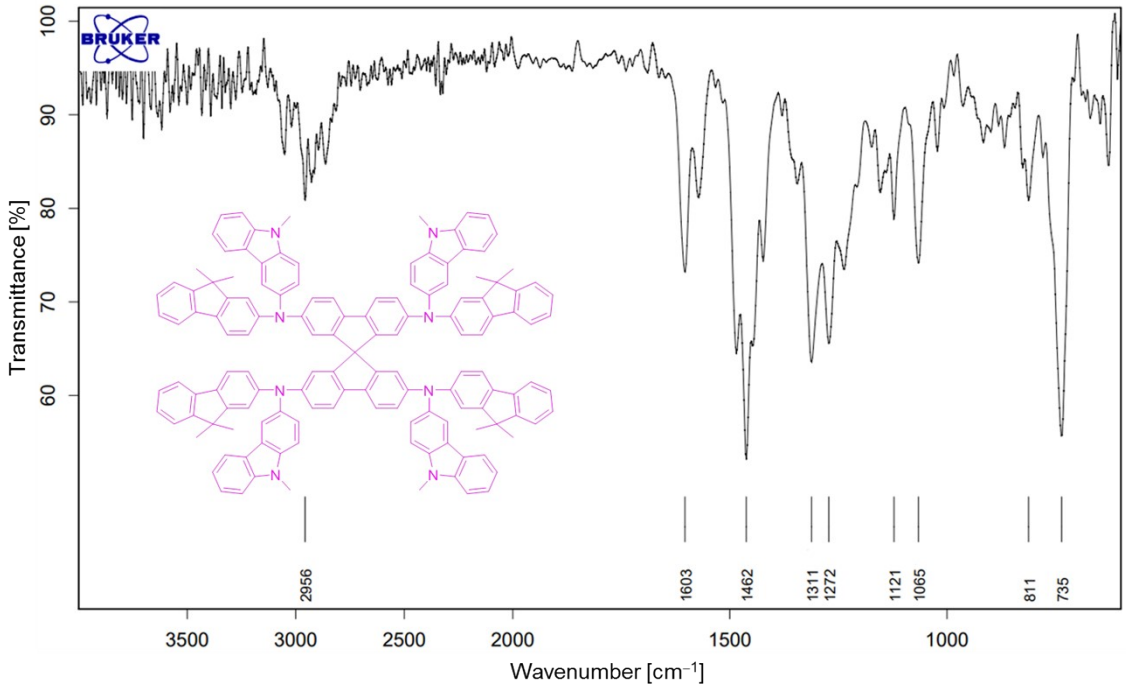

Fig. S19 ATR-FTIR spectrum of **SBF-FC**.